JACS
JOURNAL OF THE AMERICAN CHEMICAL SOCIETY
Article
pubs.acs.org/JACS

Atomistic Insights into the Conversion Reaction in Iron Fluoride: A Dynamically Adaptive Force Field Approach

Ying Ma and Stephen H. Garofalini*

Interfacial Molecular Science Laboratory, Department of Materials Science and Engineering, Rutgers University, Piscataway, New Jersey 08854, United States

ABSTRACT: Nanoscale metal fluorides are promising candidates for high capacity lithium ion batteries, in which a conversion reaction upon exposure to Li ions enables access to the multiple valence states of the metal cation. However, little is known about the molecular mechanisms and the reaction pathways in conversion that relate to the need for nanoscale starting materials. To address this reaction and the controversial role of intercalation in a promising conversion material, FeF_2, a dynamically adaptive force field that allows for a change in ion charge during reactions is applied in molecular dynamics simulations. Results provide the atomistic view of this conversion reaction that forms nanocrystals of LiF and Fe^0 and addresses the important controversy regarding intercalation. Simulations of Li^+ exposure on the low energy FeF_2 (001) and (110) surfaces show that the reaction initiates at the surface and iron clusters as well as crystalline LiF are formed, sometimes via an amorphous Li−F. Li intercalation is also observed as a function of surface orientation and rate of exposure to the Li, with different behavior on (001) and (110) surfaces. Intercalation along [001] rapid transport channels is accompanied by a slight reduction of charge density on multiple nearby Fe ions per Li ion until enough Li saturates a region and causes the nearby Fe to lose sufficient charge to become destabilized and form the nanocluster Fe^0. The resultant nanostructures are fully consistent with postconversion TEM observations, and the simulations provide the solution to the controversy regarding intercalation versus conversion and the atomistic rationale for the need for nanoscale metal fluoride starting particles in conversion cathodes.

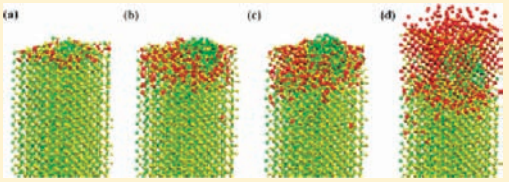

INTRODUCTION

While universally employed in energy storage,[1] commercial lithium ion batteries (LIBs) have a limited energy density in the 120−150 mAh/g range caused by the use of layered compounds as the cathode material[2] that depends on Li intercalation and that use only one unit valence change per cation. A fundamentally different approach that utilizes multiple valence states of the metal ions, as in metal fluorides,[3] is possible via the following "conversion" reaction[3c]

$$ny\mathrm{Li}^+ + \mathrm{M}_x\mathrm{X}_y + ny\mathrm{e}^- \leftrightarrow y\mathrm{Li}_n\mathrm{X} + x\mathrm{M} \quad (1)$$

where M is the metal cation and X is the anion, enabling more Li per metal cation. For cathode materials, iron fluoride (FeF_2) and iron trifluoride (FeF_3) are poor candidates as bulk materials[4] but are promising candidates as nanoparticles, having specific capacities reaching as high as 540 and 620 mAh/g, respectively.[5] However, the precise molecular mechanisms and pathways for the conversion reactions are not known, thus inhibiting a fundamental understanding that could be used to optimize these materials and extend the technology to new materials. In addition, there is controversy regarding possible Li intercalation into FeF_2, since the reduction of Fe^{2+} to Fe^{1+} is unlikely. However, an initial lithium intercalation was observed in NMR studies of FeF_2 that was attributed, without justification, to the possible presence of Fe^{3+} impurities,[2] followed by conversion and formation of LiF and Fe^0. A more recent study employing various characterization methods including high-resolution transmission electron microscopy (HRTEM), electron energy-loss spectroscopy (EELS), and X-ray pair distribution function (PDF) analysis revealed the local structural and phase evolution during the conversion, and no intercalation was observed.[6] The seemingly contradictory experimental efforts call for further investigations to resolve the role of intercalation in the conversion reaction in FeF_2. Unfortunately, the ultrafine nanograins as well as the light constituent elements make it extremely difficult to determine unambiguously the microscopic reaction mechanisms by currently available characterization techniques.

In order to address the questions regarding conversion reactions in FeF_2 and the difficulty in modeling the change in charge on the Fe from Fe^{2+} to Fe^0 as a function of Li insertion, we have enhanced a new variable charge potential[7] based on the electronegativity equalization principle,[8] creating a dynamically adaptive approach in molecular dynamics (MD) simulations. With this approach, the bond interaction evolves continuously between ionic and metallic bonds as functions of atomic charges such that the interatomic forces on each ion are fully dynamical with respect to its local geometry and connectivity. Using this dynamically adaptive force field, the conversion reaction in FeF_2 exposed to Li ions has been studied, and an unambiguous atomistic reaction pattern that results in nanostructures similar to postreaction high-resolution TEM results has been revealed.

Received: February 18, 2012
Published: April 30, 2012

   dx.doi.org/10.1021/ja301637c | J. Am. Chem. Soc. 2012, 134, 8205−8211

COMPUTATIONAL METHODS

To enable a dynamical description of the conversion reaction using MD simulation, a few difficulties have to be addressed. The first difficulty comes from the fact that multiple phases with multiple valence states are involved in the reaction. For example, the forward reaction in FeF_2 involves the formation of metallic iron and crystalline lithium fluoride (LiF), and the charge on Fe is reduced from +2 in FeF_2 to 0 in Fe metal. On the basis of the electronegativity equalization principle, a transferrable variable charge potential has been developed which is able to describe all the phases involved in the reaction with a single set of parameters, the details of which have been previously published.[7]

The second difficulty is related to the very different bonding characteristics between ionic FeF_2 and metallic Fe. For example, the Fe−Fe interaction in FeF_2 is described by the electrostatic interaction, which is evaluated by a modified Wolf summation approach[9] in a shifted damped form,[10] plus the short-range repulsion

$$V_{\mathrm{Fe-Fe}} = V^{\mathrm{rep}} + V^{\mathrm{ele}} \tag{2}$$

where

$$V^{\mathrm{rep}} = A_{ij}\exp(-r_{ij}/\rho_{ij}) \tag{3}$$

$$V^{\mathrm{ele}} = q_i q_j\left(\frac{1}{r_{\mathrm{eff}}} - \frac{1}{r_{ij}} + \frac{erfc(r_{ij}/\beta)}{r_{ij}} - \left(\frac{1}{R_{\mathrm{effc}}} - \frac{1}{R_c} + \frac{erfc(R_c/\beta)}{R_c}\right)\right) \tag{4}$$

There are a number of potentials available for Fe metal with different crystal structures. Most of these potentials fall in the category of the embedded atom method (EAM). In this work, a relatively simpler Morse type potential is used which is able to describe the body-centered cubic structure of iron:[11]

$$V_{\mathrm{Fe-Fe}} = D_0\{\exp[K_0(1 - r_{ij}/R_0)] - 2\exp[K_0/2(1 - r_{ij}/R_0)]\} \tag{5}$$

The potential energy functions for Fe−Fe in FeF_3, FeF_2, and Fe metal plotted in Figure 1 clearly show the different nature in bonding.

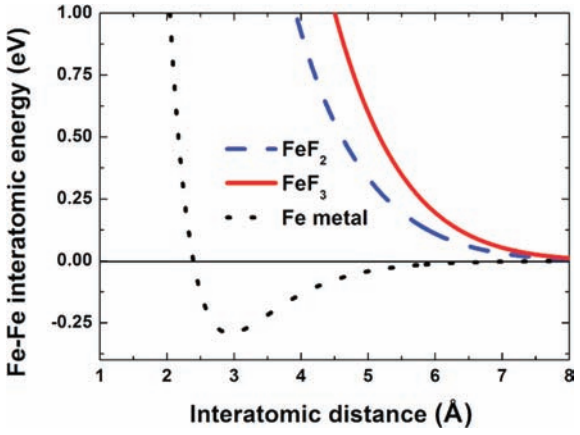

Figure 1. Fe−Fe potential energy function in FeF_3, FeF_2, and Fe metal.

To allow for a continuous transition from the ionic interactions between Fe in FeF_2 to the metallic bond in iron metal, a charge dependent function, f, is introduced:

$$f = \frac{1}{2}erfc\left(\left(\frac{q_i + q_j}{2} - 0.50\right)/0.22\right) \tag{6}$$

The potential energy function for Fe−Fe interaction is then written as

$$V_{\mathrm{Fe-Fe}} = (1 - f)V^{\mathrm{rep}} + fV^{\mathrm{M-S}} + V^{\mathrm{ele}} \tag{7}$$

In FeF_2 (and FeF_3), f approaches 0, and eq 7 is reduced to eq 2. However, when conversion starts and the charges on Fe are reduced to around 0, f approaches 1, and eq 7 is then reduced to eq 5. Similarly, a second function, f', is used to allow changes in the Fe−F interaction as the valence states of Fe changes:

$$f' = 1 - erfc\left(\frac{q_{\mathrm{Fe}} - 0.6}{3}\right) \tag{8}$$

and

$$V_{\mathrm{Fe-F}} = V^{\mathrm{rep}} + f'V^{\mathrm{M-S}} + V^{\mathrm{ele}} \tag{9}$$

Since the valence states on F and Li ions do not experience such transitions as in the case of Fe, no charge dependent functions are introduced for F−F, Li−F, and Li−Li interaction, and the forms of the potential energy functions have been described previously.[7] As such, the interatomic interactions are adaptive to the dynamically changing environments during an electrochemical conversion, which we refer to as the dynamically adaptive force field approach. The current method deals with only the atomistic level, and the switching functions are charge dependent and are designed to account for changes in the interatomic potentials during bond breaking and bond formation empirically. In this sense, the present method bears some similarities with the charge-optimized many-body (COMB)[12] potential and the reactive force field (ReaxFF)[13] method which are both EEM-based methods and can, in principle, describe the difference in the bond nature as well as breaking and formation of chemical bonds. The major advantage of the current method is that the potential has a relatively simpler form with a straightforward physical basis, which minimizes the number of empirical parameters required.

The parameters for FeF_3, FeF_2,[7] and Fe metal[11] have been reported, and the parameters for LiF are listed in Table 1. Also note that the atomic electronegativity and hardness values of Fe have been modified after the introduction of the f and f' functions such that the equilibrium charge distributions are the same as previously reported. The atomic electronegativity and hardness values are listed in Table 2.

Table 1. Parameters for the Two-Body Interactions

	Li−Li	F−F	Li−F
A_{ij} ($\times 10^{-8}$ ergs)	0.658	0.422	0.205
ρ_{ij} ($\times 10^{-8}$ cm)	0.25	0.26	0.19
D_0 ($\times 10^{-12}$ ergs)			0.48
K_0			5.62
R_0 ($\times 10^{-8}$ cm)			1.95
ζ ($\times 10^{7}$ cm^{-1})	8.95	7.59	7.83

Table 2. Atomic Electronegativity and Hardness Parameters

	χ_0 (eV)	η_0 (eV)
Fe	8.08	4.72
F	14.31	8.91
Li	6.35	6.15

It should be noted that since the functions f and f' given in eqs 6 and 9 are charge dependent, proper derivatives with respect to charge have to be evaluated when calculating the instantaneous electronegativity to ensure energy conservation. In principle, any EEM based methods may suffer from a serious energy drift problem due to the nonvanishing $(\partial q)/(\partial r)$ term.[8d] In practice, the effect of this term is negligible once the equilibrium electronegativity is sufficiently converged. MD simulations under the microcanonical ensemble show no sign of energy drift during a typical simulation length of 30 ps.

Using this approach, two types of MD simulations are performed: constrained MD and unconstrained, or normal, MD simulations.

dx.doi.org/10.1021/ja301637c | J. Am. Chem. Soc. 2012, 134, 8205−8211

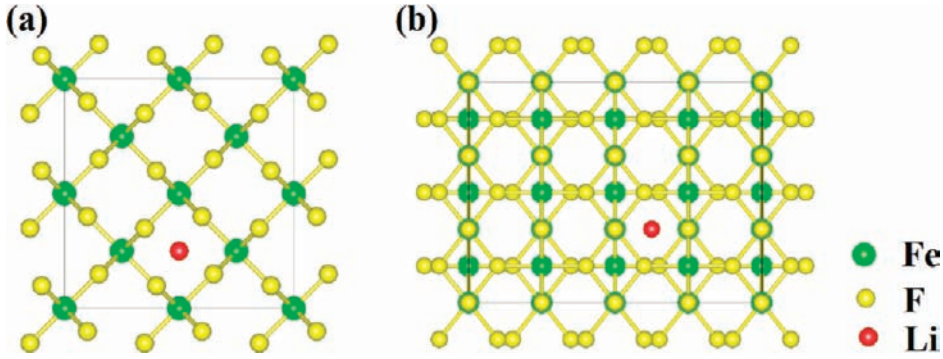

Figure 2. Top view of the [001] and [110] channels in FeF_2.

A time step of 1 fs is used, 3D periodic boundary conditions (PBC) are used for the bulk simulations, and PBC in only the x and y dimensions are used in the conversion reactions. Bulk simulations employ a 28 × 28 × 28 Å^3 FeF_2 crystal, while a 28 × 28 × 66 Å^3 and a 26 × 29 × 66 Å^3 dimension is used for (001) and (110) surfaces, respectively, with a 100 Å thick vacuum above the free surface and the bottom 10 Å of the crystal frozen. Both FeF_2 surface systems contain 4320 atoms. Constrained MD simulations are used to calculate the activation barriers for Li ion diffusion along open channels in [001] and [110] directions in the FeF_2 bulk crystal. The constraint is with regard to the added Li ion. In these cases, a lithium ion is moved incrementally 0.1 Å parallel to the channel (e.g., z direction) and held at that z position for 2000 iterations at 10 K, but allowed to relax in the plane perpendicular to the channel (e.g., x–y); all other atoms in the system were allowed to relax. The average energy at each incremental position is calculated. The use of 10 K removes the noise that would occur at room temperature.

In the simulations of the conversion reaction on the surface, normal MD simulations are used. In addition, to keep Li^+ ions from migration into the vacuum above the exposed surface, a reflecting boundary is added around 2 Å above the surface, and lithium ions are randomly generated at a specific rate along the reflecting boundary to simulate Li^+ insertion. The position of the reflecting boundary increases with the increase of number of Li ions to allow for possible volume expansion during conversion. Temperature rescaling is applied along the reflecting boundary and the bottom 20 Å (excluding frozen atoms) to mimic heat dissipation through a presumed carbon matrix.

First principles calculations have also been used to obtain the Bader charges around a Li ion in FeF_2 crystal. The calculations are performed within the density functional theory (DFT) using a plane wave basis set as implemented in the Vienna *ab initio* simulation package (VASP).[14] The projector augmented wave method[15] is used, and the exchange correlation potential is described by a generalized gradient approximation with the Perdew–Burke–Ernzerhof parametrization.[16] Charge densities are first calculated using VASP, from which Bader charges are obtained.[17]

RESULTS

Geometrical analysis suggests that diffusion channels exist along both [001] and [110] directions, as shown in Figure 2, implying possible intercalation of Li^+ into FeF_2. The diffusion barriers along both channels were determined using constrained molecular dynamics simulations. The calculated barriers confirmed our expectation as shown in Figure 3. Indeed, the barrier along [001] channel is only 0.05 eV. Such a small barrier is confirmed by a first principles nudged elastic band (NEB) calculation which gives a barrier of 0.09 eV. Even though the barrier along [110] is much higher (around 1.0 eV), the extremely low barrier along the [001] channel could support fast Li^+ transport and intercalation that is usually believed to be absent in FeF_2 because of the inability of the Fe^{2+} ion to attain a

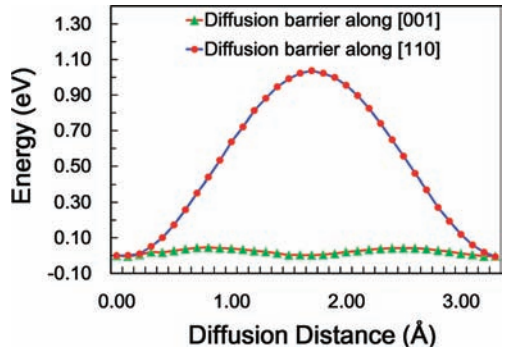

Figure 3. Lithium ion energies as functions of diffusion distance in bulk FeF_2 crystal along [001] and [110] channels.

stable Fe^{1+} state. The assumption is that the presence of a Li^+ ion causes an adjacent Fe^{2+} ion to attain the Fe^{1+} state.

To determine the effect of exposure of FeF_2 to Li^+, further MD simulations of Li^+ diffusion into the (001) and (110) surfaces are carried out. Two Li exposure rates were used: 72 Li^+ every 20 ps (fast rate) and a 4× slower rate of 9 Li^+ every 10 ps (slow rate). Figures 4, 5, and 6 show snapshots of the structural evolution as a function of time (number of Li^+ added to the surface) for different conditions. Figure 4 shows the results for the (001) oriented FeF_2 crystal for the "fast rate" reaction, Figure 5 shows the same for the "slow rate" reaction, and Figure 6 shows the results for the "slow rate" reaction for the (110) oriented FeF_2 crystal (the "fast rate" for the (110) is similar to that of the "slow rate" and is not shown). In all cases, with the initial addition of Li^+, the charge on the Fe ions near the surface quickly decreases to <1.0, which destabilizes the Fe–F bonds and, with the presence of Li ions, causes their rupture and formation of Li–F bonds and migration of those Fe ions to form an Fe^0 (metal) nanocluster.

In Figure 4, the (001) "fast rate" simulation, some minor intercalation of Li^+ occurs, but the destabilization of the Fe^{2+} is rapid as its charge is reduced, and because of the number of Li^+ randomly added above the surface, an amorphous Li–F structure forms as the metal cluster (Fe^0) forms (part b). After a stoichiometrically sufficient number of Li^+ adsorbs, the amorphous Li–F transforms into the crystalline LiF (part d). Because of the fast rate of Li^+ exposure, the conversion to the LiF crystal occurs prior to significant migration of Li^+ down the low-barrier [001] channel. After the upper surface converts to crystalline LiF, further Li^+ penetration into the conversion zone is severely inhibited, consistent with its low ionic conductivity, thereby limiting the amount of conversion. The implication is that a slower rate of exposure might cause more Li^+ to

dx.doi.org/10.1021/ja301637c | J. Am. Chem. Soc. 2012, 134, 8205–8211

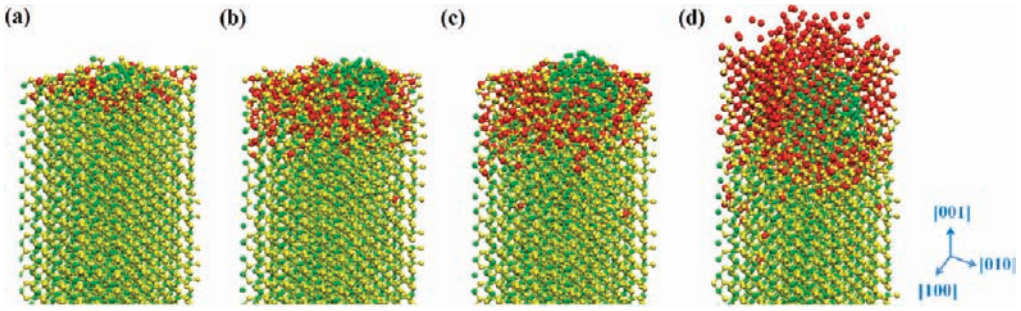

Figure 4. Reaction on the (001) surface with the "fast rate". Atom colors as in Figure 2: Fe–F bond is yellow, and Li–F bond is red. (a) System with 72 Li^+ already shows the growth of Fe metal cluster. (b) 288 Li^+ with a glassy Li–F region. (c) 360 Li^+, crystalline LiF observed at the left corner. (d) 864 Li^+, crystalline LiF grows.

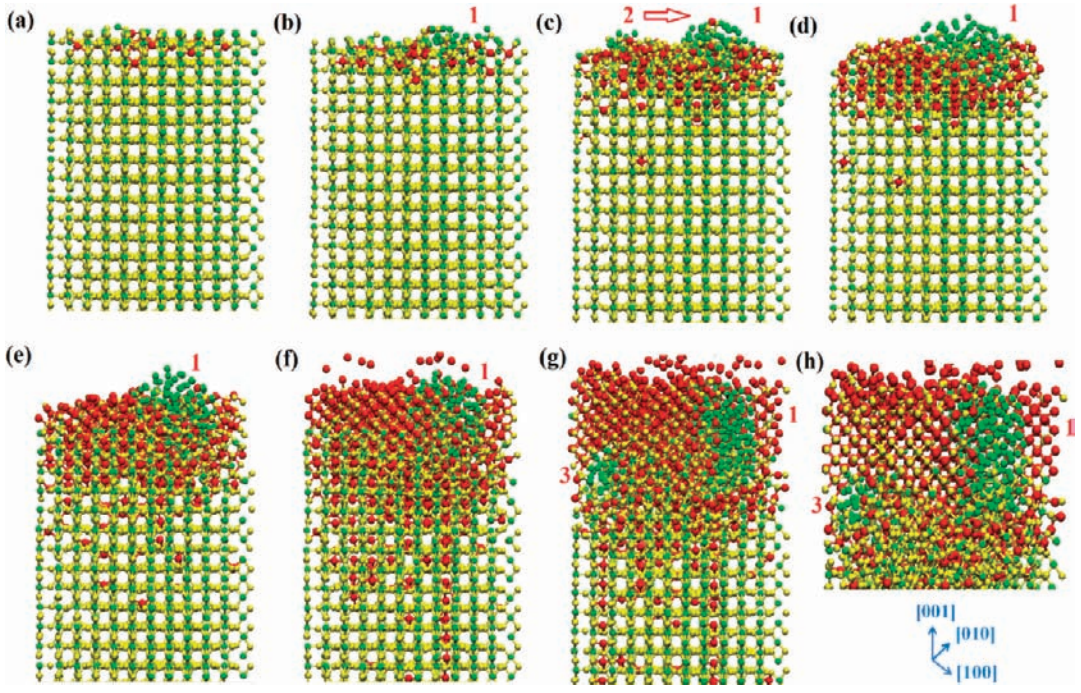

Figure 5. Atomistic pattern of the conversion reaction on the (001) surface of FeF_2 at the "slow rate"; color scheme given in Figure 2. (a) Lithium immediately adsorbs subsurface. (b) Surface Fe destabilized, forming the first Fe^0 cluster on the surface (labeled 1). (c) The second Fe cluster (2) forms and is attracted to the first one. (d) The first Fe cluster grows, and a glassy Li–F forms on the surface as additional Li intercalate down channels. (e) The crystalline LiF phase nucleates on the surface. (f) Li^+ insertion is slowed down by the LiF crystal, and lithium ions accumulate above the surface. (g) LiF continues to grow, and the third Fe cluster forms subsurface (3). (h) The top region in part g enlarged and slightly rotated around [001] to more clearly see the nanocrystalline LiF. Arrow in part b indicates that the second Fe cluster is attracted to the first one.

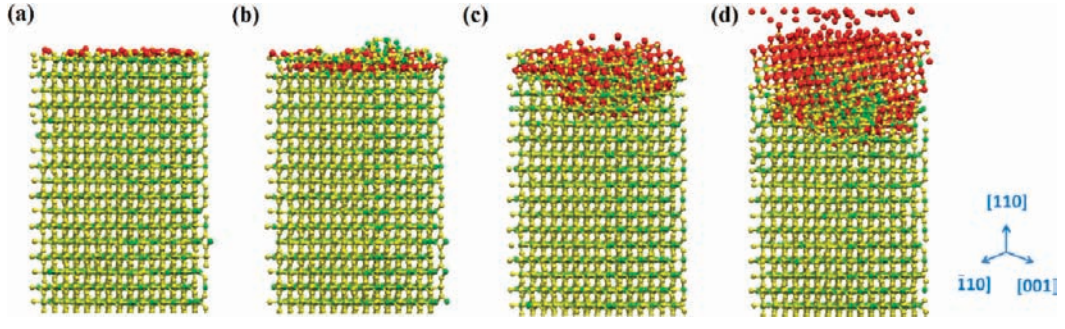

Figure 6. Conversion reaction on the (110) surface of FeF_2; color scheme as in Figure 2. (a) Lithium ions initially adsorb on the top of the surface, but in part b rapidly move to second layer subsurface as an Fe cluster nucleates on surface. (c) LiF crystal nucleates as Fe cluster grows subsurface and some Li^+ migrate below the Fe crystal. (d) LiF crystal grows on top of the Fe cluster, although Li^+ insertion is slowed down by the LiF crystal, causing added Li to accumulate above the surface.

dx.doi.org/10.1021/ja301637c | *J. Am. Chem. Soc.* 2012, 134, 8205–8211

intercalate through the amorphous Li−F into the subsurface prior to the conversion to the LiF crystal.

To test this implication, the structural evolution for the "slow rate" exposure on the (001) surface was evaluated, and as Figure 5 shows, the low diffusion barrier along the (001) channel enables some Li^+ penetration into the third layer subsurface as the Fe^0 metal cluster (labeled 1 in Figure 5b) forms. Li^+ penetration is sufficiently rapid that some have entered the fourth layer as more surface Fe ions are reduced to a zero charge state and a second Fe^0 cluster forms on the surface (labeled 2 in Figure 5c). This second Fe^0 cluster quickly diffuses over the surface and merges with the first metal cluster (Figure 5d). At the same time, amorphous Li−F forms near the surface and more Li^+ ions enter the (001) channels and destabilize additional Fe ions that then move to the metal cluster. This intercalation was not believed to occur in FeF_2 because of the view that the Li ion adds an accompanying −1 charge to the adjacent Fe, but the Fe cannot attain the Fe^{1+} state. However, analysis of the charge distribution around a lithium ion inserted into the [001] channel of FeF_2 suggests an alternative point of view, as shown in Figure 7. Both MD

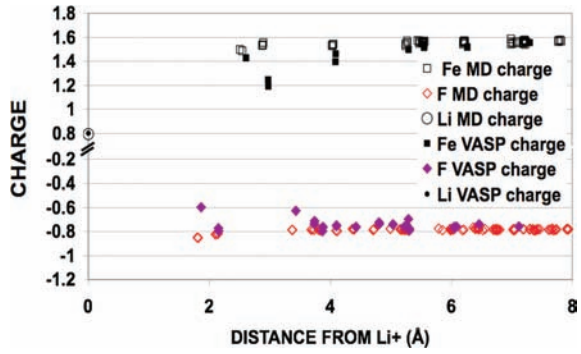

Figure 7. MD and VASP charge distribution on ions around a single Li^+ located in the [001] channel of FeF_2. Only ions closest to Li^+ are affected, with no Fe reduced to 50% of charge by a single nearby Li^+.

charges and first principles Bader charges from VASP-DFT calculations are shown, although a much smaller system size is used in VASP calculation due to computational restrictions. In both cases, the negative charge density (an electron) accompanying lithium insertion is distributed among multiple Fe ions close to the center Li^+ so that no one Fe^{2+} reaches the +1 state. Further analysis shows that only with multiple nearby Li in the channel does the charge density on neighboring Fe decrease sufficiently so that the Fe ions are unstable in their lattice sites and break Fe−F bonds and migrate to form the metal cluster in the Fe^0 state. The implication of such an observation is that intercalation is supported prior to the formation of metal clusters.

Unlike the "fast rate" reactions, the slower exposure to Li ions and the low barrier in the [001] direction allow more Li^+ to diffuse into the FeF_2 subsurface (Figure 5e−g), essentially preventing a stoichiometric concentration of Li^+ in the conversion zone to form the LiF crystal in the early stages of adsorption, enabling formation of the amorphous Li−F while allowing for growth of the metal cluster. Eventually, an increase in the Li^+ in the surface region enables formation of crystalline LiF (parts f and g) and, with earlier Li^+ in the subsurface channels, formation of a third Fe^0 cluster (labeled 3 in part g) below the LiF crystal. The LiF crystal is more easily seen in the rotated and expanded view in Figure 5h. Again, formation of crystalline LiF at the surface slows further adsorption of Li^+ from above.

As depicted in Figure 6, the "slow rate" reaction pattern on the (110) surface is quite different from the (001) surface. Because of the higher barrier for Li^+ diffusion in the [110] direction, no intercalation is observed. Rather, Li^+ ions destabilize the Fe in the upper layers, enabling nucleation of the Fe^0 metal cluster while the Li^+ ions bond to the F in the layer. This destabilization creates vacancies and allows the Li^+ to diffuse into the next lower layer (Figure 6b), followed by similar progress into the subsurface in a layer-by-layer process (Figure 6b−d). As the Fe^0 -cluster grows, Li^+ ions also penetrate below the Fe^0-cluster via migration along the interface between the metal cluster and the fluoride. Because this is a restricted layer-by-layer process, stoichiometric LiF is attained at the surface (part c) and no large scale amorphous Li−F forms as it does on the (001) surface. Crystalline LiF eventually forms around the Fe^0 metal cluster, slowing further adsorption of Li ions from above (Figure 6d).

DISCUSSION

Rapid conversion is observed for both surfaces even though the diffusion barriers are very different. On both surfaces in our simulations, Fe^0 clusters with diameters around 2−3 nm are formed. These features are consistent with a recent experimental observation of the bicontinuous network of metallic Fe^0 particles with diameters less than 5 nm after conversion.[6] The Fe^0 cluster nucleates after Li^+ adsorption around 60% of the Fe ions in a monolayer of FeF_2. A major reason is that the charge on Fe ions of the top 1−2 layers is significantly reduced due to the change of bonding at the surface,[7] the addition of lithium ions quickly reduces the charges on those Fe ions to around zero, and an Fe^0 cluster starts to form. Fe ions below are then exposed to additional lithium ions after the formation of this initial Fe^0 cluster. These ions are also reduced and attracted to the cluster, and the cluster grows. This is especially true in the case of the (110) surface, where the activation barrier for Li diffusion down the [110] channel is high. In the case of the (001) surface, more lithium ions penetrate deeper into the FeF_2 subsurface, and some channels are filled within the current simulation, so intercalation is simultaneous with conversion at low exposure rates. After formation of the LiF crystal, the reaction slows down since fewer lithium ions are able to diffuse close to unconverted Fe layers and the charges on those Fe ions cannot be reduced effectively. It is expected that a complete conversion would require building up of sufficient lithium ions below already-formed LiF crystals and Fe^0 clusters in order to convert subsurface Fe.

These observations are further confirmed by analyzing an instantaneous charge distribution on the atoms in the system. In Figure 8 the charge distribution along the surface norm for the structure depicted in Figure 5g is plotted. Three different regions can be identified. Below 10 Å is the frozen crystal, and the charges on ions in this region assume their respective bulk values. Between 42 and 66 Å (around 24 Å below the surface) is the conversion reaction region, which is characterized by the formation of metallic iron clusters with zero charge state. It is interesting to point out that the charges on Fe ions in this region either remain close to their bulk value (∼1.6) or decrease close to the value in the Fe cluster (∼0). Since a fractional charge model is employed in the current work, a 1.6 charge value actually corresponds to +2 valence state for Fe.

dx.doi.org/10.1021/ja301637c | J. Am. Chem. Soc. 2012, 134, 8205−8211

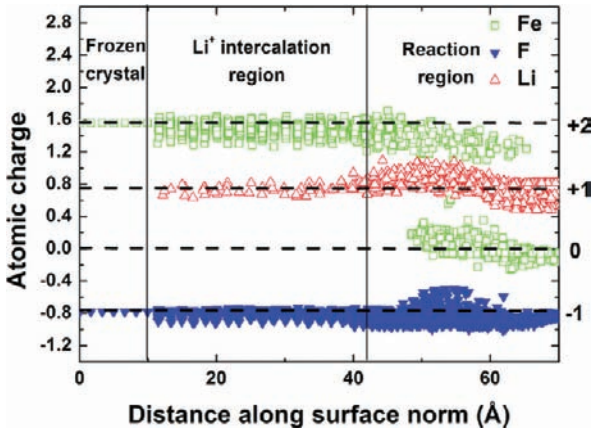

Figure 8. Charge distribution along the surface norm for the configuration shown in Figure 5g. Horizontal dashed lines correspond to nominal +2, +1, 0, and −1 valence states. Vertical solid lines separate the system into three different regions (see text).

Similarly, the 0.8 and −0.8 charge values correspond to +1 and −1 valence states. Few intermediate (+1) valence states are observed for the Fe. Tracking of the charge evolution on an Fe ion shows that the +1 valence state (0.8 charge) is quite unstable and is quickly reduced further to the zero state. Hence, the figure can contain some fleeting charges that are changing with the local configuration. In between the frozen crystal and the reaction region is the intercalation region, where lithium intercalation and diffusion along the [001] channels are observed (Figure 5g). To compensate the extra charges on the intercalating Li^+, charges on most Fe ions in this region decrease slightly. Thus, the introduction of Li^+ ions leads to a distortion of the local electronic structure distributed over several nearby Fe, rather than the full reduction of an individual Fe ion. The net effect of such a distortion is the reduced Fe−F attraction, i.e., the increased structural instability of FeF_2. Since further Li^+ insertion is blocked by the LiF crystal formed above, the charges on Fe ions cannot be further reduced, thus forming a stable intercalation region. However, it is expected that Fe reduction and continued reaction would occur once enough Li^+ ions diffuse into this region, for example, when a slower discharging rate is used. In other words, the local Li^+ concentration drives the conversion reaction. When the concentration is high enough, charges on multiple Fe ions will be effectively reduced to zero, the local FeF_2 structure is no longer stable and the conversion reaction starts. This is seen in Figure 5g, where a third Fe-metal cluster forms subsurface as the Fe species in the local FeF_2 crystal are all reduced sufficiently. On the surface, since the charges on Fe are already reduced,[7] the required Li^+ concentration is smaller. The larger diffusion barrier along the [110] channel also helps to build a sufficient Li^+ concentration. As a result, rapid conversion is first observed on the (110) surface. It should be noted that the current study made no attempt toward identifying the electronic conduction pathways, which is clearly beyond the scope of any MD methods. The EEM approach actually assumes a zero electronic conduction barrier, and at each simulation step, the appropriate number of electrons would enter into the system in conjunction with the inserted Li^+ ions and reach the equilibrium distribution. Such an assumption may seem unreasonable since FeF_2 is a wide band gap insulator. However, the use of nanoparticles could support appreciable electron transport due to the reduced path length as well as the increased possibility of electron tunneling. Furthermore, Li^+ insertion and defects could create band gap levels that facilitate electron hopping.

Since the current simulations involved PBC in the dimensions perpendicular to the exposed surfaces, penetration of Li^+ along multiple directions, as would occur in a nanoparticle, cannot occur. In a nanoparticle, the additional penetration path from an exposed (001) surface would offer Li^+ to the lower conversion region of the (110) surface, allowing for continued reaction along both surfaces. Such results help explain the experimentally observed requirement of using FeF_2 nanoparticles versus larger particles for these conversion reactions.

The discharging rate also plays an important role. The simulations show that an increase in the discharge rate leads to a decrease of the penetration depth, even for the (001) surface where only a few lithium ions are observed below the converted region if the discharging rate is too fast and crystalline LiF forms on the surface prior to significant intercalation. If a large discharge rate is used, the full capacity of the battery cannot be achieved since the region below the surface may not react. However, given a sufficiently low rate it is expected that more lithium ions will penetrate deeper into the particles to ensure a more continuous conversion reaction. Therefore, the current simulations reveal that an important reason in restricting the discharging rate is the formation of the LiF crystal on the surface that inhibits further lithium diffusion necessary for continued conversion reaction.

The actual reaction pattern observed experimentally would then depend on the actual shape, size of the nano-FeF_2 particle, as well as the discharging rate. Although both (001) and (110) are low energy surfaces, the (110) surface energy is around 70% of that of the (001) surface.[7] It is then expected that the equilibrium shape of the FeF_2 nanoparticle is dominated by the (110) surface. The reaction on the (110) surface is quite rapid, and a well ordered crystalline LiF phase is expected to grow into the (110) surface at the earlier stages of the reaction. For the reaction to continue, it is then important that the discharging rate should be sufficiently low such that enough Li^+ can diffuse into the particle along exposed (001) channels in the nanoparticle toward the lower conversion region of the (110) surfaces, thus continuing the conversion. Eventual formation of the LiF crystal on the (001) surface would significantly slow the conversion process in the nanoparticle. Therefore, the simulations indicate that conversion reactions would occur while simultaneous intercalation occurs so that intercalation might be experimentally difficult to observe. Intercalation is possible because the compensating negative charge associated with a specific Li^+ ion is distributed among several lattice ions, thus lowering the charge on a specific neighboring Fe^{2+} less than that needed for it to reach the destabilizing state unless multiple Li^+ species are near that Fe^{2+} ion.

■ CONCLUSIONS

In conclusion, the conversion reaction occurring in crystalline FeF_2 surfaces exposed to Li^+ ions has been studied using a dynamically adaptive force field approach that modifies charges and interaction potentials in response to the local atomistic environment. The conversion from $FeF_2 + Li^+$ to nanocrystalline LiF and Fe^0 and the competition between conversion and intercalation on (001) and (110) FeF_2 surfaces have been identified and compared. The simulations show the importance

dx.doi.org/10.1021/ja301637c | J. Am. Chem. Soc. 2012, 134, 8205−8211

of crystal surface orientation and discharging rate on conversion and intercalation, with an explanation for the presence of intercalation concurrent with conversion. These simulations demonstrate the need for the use of nanoparticles as starting materials for conversion devices and the role intercalation plays on continued reactions and high capacity.

AUTHOR INFORMATION

Corresponding Author

shg@rutgers.edu

Notes

The authors declare no competing financial interest.

ACKNOWLEDGMENTS

The authors acknowledge Min-Hua (Ivy) Chen and Prof. Van de Ven at the University of Michigan for providing first principles NEB data. This work is financially supported by the Northeastern Center for Chemical Energy Storage, an Energy Frontier Research Center, funded by the U.S. Department of Energy, Office of Basic Energy Sciences, under award contract DE-SC0001294.

REFERENCES

(1) (a) Mizushima, K.; Jones, P. C.; Wiseman, P. J.; Goodenough, J. B. *Mater. Res. Bull.* **1980**, *15* (6), 783−789. (b) Brodd, R. J. Lithium-Ion Batteries: Science and Technology. In *Lithium-Ion Batteries: Science and Technology*; Yoshio, M.; Brodd, R. J.; Kozawa, A. Eds.; Springer: New York, 2009; p 1. (c) Tarascon, J. M.; Armand, M. *Nature* **2001**, *414* (6861), 359−367.

(2) Yamakawa, N.; Jiang, M.; Key, B.; Grey, C. P. *J. Am. Chem. Soc.* **2009**, *131*, 10525−10536.

(3) (a) Li, H.; Richter, G.; Maier, J. *Adv. Mater.* **2003**, *15* (9), 736−739. (b) Li, H.; Balaya, P.; Maier, J. *J. Electrochem. Soc.* **2004**, *151* (11), A1878−A1885. (c) Cabana, J.; Monconduit, L.; Larcher, D.; Palacin, M. R. *Adv. Mater.* **2010**, *22* (35), E170−E192.

(4) Arai, H.; Okada, S.; Sakurai, Y.; Yamaki, J. *J. Power Sources* **1997**, *68* (2), 716−719.

(5) (a) Badway, F.; Cosandey, F.; Pereira, N.; Amatucci, G. G. *J. Electrochem. Soc.* **2003**, *150*, A1318−A1327. (b) Badway, F.; Pereira, N.; Cosandey, F.; Amatucci, G. G. *J. Electrochem. Soc.* **2003**, *150*, A1209−A1218. (c) Cosandey, F.; Al-Sharab, J. F.; Badway, F.; Amatucci, G. G.; Stadelmann, P. *Microsc. Microanal.* **2007**, *13* (2), 87−95. (d) Amatucci, G. G.; Pereira, N. *J. Fluorine Chem.* **2007**, *128* (4), 243−262.

(6) Wang, F.; Robert, R.; Chernova, N. A.; Pereira, N.; Omenya, F.; Badway, F.; Hua, X.; Ruotolo, M.; Zhang, R.; Wu, L.; Volkov, V.; Su, D.; Key, B.; Whittingham, M. S.; Grey, C. P.; Amatucci, G. G.; Zhu, Y.; Graetz, J. *J. Am. Chem. Soc.* **2011**, *133* (46), 18828−18836.

(7) Ma, Y.; Lockwood, G. K.; Garofalini, S. H. *J. Phys. Chem. C* **2011**, *115* (49), 24198−24205.

(8) (a) Sanderson, R. T. *Chemical Bonds and Bond Energy*; Academic Press: New York, 1976. (b) Mortier, W. J.; Van Genechten, K.; Gasteiger, J. *J. Am. Chem. Soc.* **1985**, *107* (4), 829−835. (c) Parr, R. G.; Yang, W. *Density Functional Theory of Atoms and Molecules*; Oxford University Press: Oxford, 1989. (d) Ma, Y.; Garofalini, S. H. *J. Chem. Phys.* **2006**, *124*, 234102.

(9) (a) Wolf, D.; Keblinski, P.; Phillpot, S. R.; Eggebrecht, J. *J. Chem. Phys.* **1999**, *110*, 8254−8282. (b) Ma, Y.; Garofalini, S. H. *Mol. Simul.* **2005**, *31*, 739−748. (c) Ma, Y.; Garofalini, S. H. *J. Chem. Phys.* **2005**, *122*, 094508−1−5.

(10) Fennell, C. J.; Gezelter, J. D. *J. Chem. Phys.* **2006**, *124*, 234104−1−12.

(11) Imamova, S. E.; Atanasov, P. A.; Nedialkov, N. N.; Dausinger, F.; Berger, P. *Nucl. Instrum. Meth. B* **2005**, *227* (4), 490−498.

(12) Yu, J. G.; Sinnott, S. B.; Phillpot, S. R. *Phys. Rev. B* **2007**, *75* (8), 085311.

(13) van Duin, A. C. T.; Strachan, A.; Stewman, S.; Zhang, Q.; Xu, X.; Goddard, W. A. *J. Phys. Chem. A* **2003**, *107*, 3803−3811.

(14) (a) Kresse, G.; Furthmuller, J. *Comput. Mater. Sci.* **1996**, *6*, 15−50. (b) Kresse, G.; Furthmuller, J. *Phys. Rev. B* **1996**, *54*, 11169−11186.

(15) Blochl, P. E. *Phys. Rev. B* **1994**, *50* (24), 17953−17979.

(16) Perdew, J. P.; Burke, K.; Ernzerhof, M. *Phys. Rev. Lett.* **1996**, *77* (18), 3865.

(17) (a) Tang, W.; Sanville, E.; Henkelman, G. *J. Phys.: Condens. Matter* **2009**, *21* (8), 804204. (b) Sanville, E.; Kenny, S. D.; Smith, R.; Henkelman, G. *J. Comput. Chem.* **2007**, *28* (5), 899−908.